Nano-optical designs enhance monolithic perovskite/silicon tandem solar cells toward 29.8% efficiency

Philipp Tockhorn
Helmholtz-Zentrum Berlin
Johannes Sutter
Helmholtz-Zentrum Berlin https://orcid.org/0000-0001-5634-3449
Alexandros Cruz
Helmholtz-Zentrum Berlin
Philipp Wagner
Helmholtz-Zentrum Berlin https://orcid.org/0000-0001-7652-9144
Klaus Jäger
Helmholtz-Zentrum Berlin
Danbi Yoo
Helmholtz-Zentrum Berlin
Felix Lang
University of Potsdam
Max Grischek
Helmholtz-Zentrum Berlin https://orcid.org/0000-0002-9786-4854
Bor Li
Helmholtz-Zentrum Berlin
Amran Al-Ashouri
Helmholtz-Zentrum Berlin
Eike Köhnen
Helmholtz-Zentrum Berlin https://orcid.org/0000-0002-3637-4907
Martin Stolterfoht
University of Potsdam
Dieter Neher
University of Potsdam
Rutger Schlatmann
Helmholtz-Zentrum Berlin
Bernd Rech
Helmholtz-Zentrum Berlin https://orcid.org/0000-0002-9718-8665
Bernd Stannowski

Helmholtz-Zentrum Berlin

Steve Albrecht

Technical University Berlin

Christiane Becker (christiane.becker@helmholtz-berlin.de)

Helmholtz-Zentrum Berlin https://orcid.org/0000-0003-4658-4358

Article

Keywords:

Posted Date: March 17th, 2022

DOI: https://doi.org/10.21203/rs.3.rs-1439562/v1

Version of Record: A version of this preprint was published at Nature Nanotechnology on October 24th, 2022. See the published version at https://doi.org/10.1038/s41565-022-01228-8.

Nano-optical designs enhance monolithic perovskite/silicon tandem solar cells toward 29.8% efficiency

Philipp Tockhorn[1#], Johannes Sutter[1#], Alexandros Cruz[1], Philipp Wagner[1], Klaus Jäger[1,2], Danbi Yoo[1], Felix Lang[3], Max Grischek[1,3], Bor Li[1], Amran Al-Ashouri[1], Eike Köhnen[1], Martin Stolterfoht[3], Dieter Neher[3], Rutger Schlatmann[1,5], Bernd Rech[1,4], Bernd Stannowski[1], Steve Albrecht[1,4], Christiane Becker[1,5]**

[1] Helmholtz-Zentrum Berlin für Materialien und Energie GmbH, Division Solar Energy, Kekuléstr. 5, 12489, Berlin, Germany

[2] Zuse Institute Berlin, Computational Nanooptics Group, Takustr. 7, 14195 Berlin, Germany

[3] Universität Potsdam, Soft matter physics, Karl-Liebknecht-Straße 24/25, 14476 Potsdam, Germany

[4]Technische Universität Berlin, Faculty of Electrical Engineering and Computer Science, 10587 Berlin, Germany

[5] Hochschule für Technik und Wirtschaft Berlin, Faculty 1: School of Engineering – Energy and Information, 10313 Berlin, Germany

# These authors contributed equally to this work. Order determined by cast of dice.

* Email: steve.albrecht@helmholtz-berlin.de, christiane.becker@helmholtz-berlin.de

Abstract – up to 150 words, unreferenced

Perovskite/silicon tandem solar cells allow to overcome the power conversion efficiency limit of market-dominating silicon solar cells. So far, various textured tandem devices were presented aiming at improved optical performance, but highest efficiencies were still realized on polished silicon wafer cells enabling superior perovskite layer properties. Here we present perovskite/silicon tandem solar cells with gentle periodic nanotextures which feature various advantages without compromising the material quality of solution-processed perovskite layers. Reflection losses are reduced in comparison to planar tandems and the devices are less sensitive upon deviations from optimum layer thicknesses. The nanotextures also enable excellent perovskite film formation and a greatly increased fabrication yield. The open-circuit voltage improved by about 15 mV due to enhanced electronic properties of the perovskite top cell. In addition, an optically advanced rear reflector with a dielectric buffer layer reduced parasitic absorption at near-infrared wavelengths. Altogether, the improvements enabled a certified power conversion efficiency of 29.80%.

Monolithic, 2-terminal perovskite/silicon tandem solar cells (PSTSC) have recently achieved power conversion efficiencies (PCE) exceeding 29%[1,2] and therefore overcome the physical limit of market-dominating crystalline-silicon single-junction solar cells[3]. Such high PCEs were reached by continuous improvements of the optical and electronic properties of PSTSC. These improvements include, amongst others, switching the cell polarity for enhanced top-contact transmission[4], and fine-tuning of various layers to improve the optical performance[5–7]. In addition, various publications addressed the improvement of the electronic properties by optimizing contact layers[1], utilizing additives[8–10] and adjusting the perovskite composition[11] or deposition[12]. Numerical studies predict a further increase of PCE with adequate light management by introducing textured device interfaces[13,14]. For silicon solar cells, potassium-hydroxide etched random pyramidal textures with a size of several micrometers are commonly used for light management. However, they are not compatible with solution-processed perovskite absorbers without further adaptation. In recent years, different approaches to implement light management textures in PSTSC were investigated, either by adapting the perovskite deposition technique but leaving the pyramidal texture unchanged[15–20] with maximum PCE of 27.4%[20], or by adapting the pyramidal textures such that perovskite solution-processing becomes feasible[10,21–25] leading to a maximum PCE of 28.6%[25] (Fig. S1). These reported PCEs are still below the best scientifically published result for PSTSCs based on perovskite absorbers spin-coated onto silicon bottom cells with flat, polished front side (29.15%)[1], mainly due to deficits of the perovskite material quality on standard and adapted pyramidal textures. Therefore, it remains a significant challenge to develop an appropriate texture, which is able to balance the persistent trade-off between electronic and optical performance of textured PSTSCs and hence allows to push the PCE beyond 30%. In recent studies we already introduced gentle sinusoidal nanotextures with sub-micrometer feature size (see Fig. 1d) as promising candidate for PSTSCs: optical simulations indicated that the PCE can be significantly enhanced compared to planar reference tandem solar cells[26]. We further demonstrated experimentally that such nanotextures provide a feasible light-management solution in both, perovskite[27] and silicon[28] single junction solar cells, without compromising the optoelectronic quality of the respective absorber.

In this work, we present PSTSCs with a gentle sinusoidal nanotexture connecting the advantages of structuring the silicon surface while preserving the material quality of the

perovskite. We show that the nanotextured devices feature a substantial reduction of reflection losses compared to their planar counterpart and a significantly reduced sensitivity against deviations from optically optimum layer thicknesses. More than that, nanotexturing strongly improves the fabrication yield enabled by the excellent film formation properties of spin-coated perovskite films on nanotextured silicon bottom cells and a statistically relevant increase of the open-circuit voltage by 15 mV is observed. In order to meet the challenge of parasitic absorption losses, we further implement a reflector with dielectric buffer layer (RDBL) at the rear side of the silicon bottom cell. This buffer layer optically decouples the contact metal and the silicon absorber[29], allows to decrease the thickness of the transparent conductive layer[30] and hence reduces parasitic absorption losses considerably. Combining both approaches, i.e. the gentle nanotexture at the front side and the reflector with dielectric buffer layer at the rear side of the silicon bottom cell, we demonstrate a monolithic PSTSC with an independently certified power conversion efficiency of 29.80%.

Tandem design

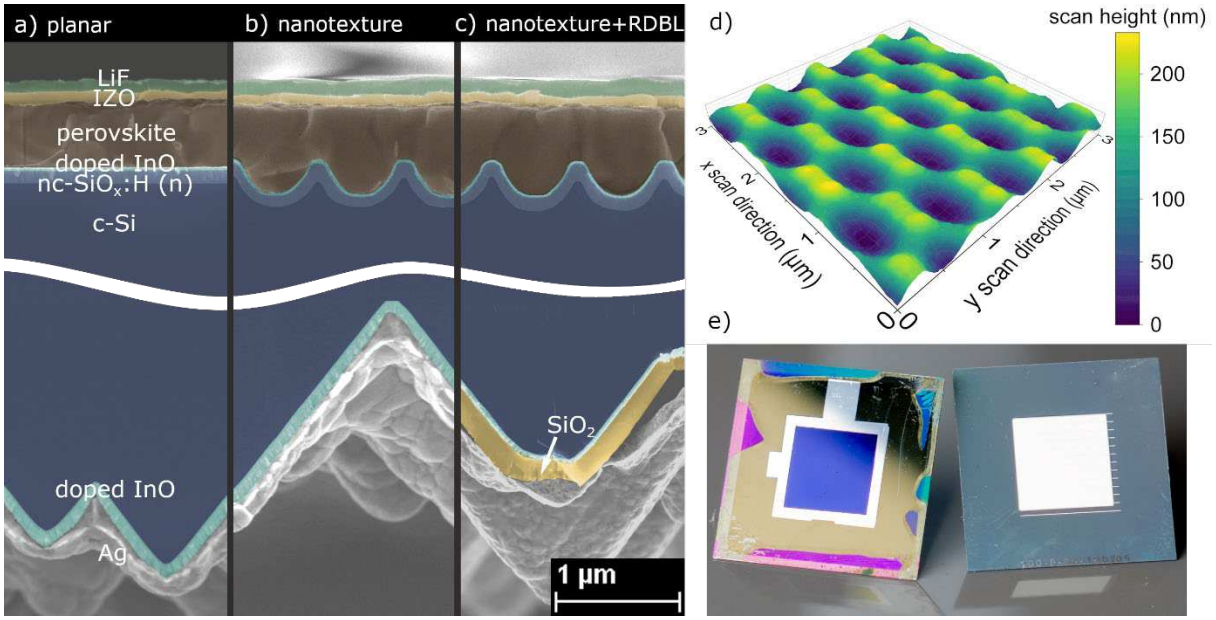

Figure 1 | Nanotextured perovskite/silicon tandem solar cell (PSTSC) design. a-c) Scanning electron microscopic (SEM) cross-section micrographs of the front and rear side for a) planar, b) nanotextured, c) nanotextured and reflector with dielectric buffer layer (RDBL) configuration. d) Atomic force microscopy (AFM) image of the nanostructured silicon bottom cell front side prior to the deposition of the contact layers. e) Photographs of the final PSTSC with a blue active area in between the frontside silver ring of approximately 1 cm^2 (left side) and RDBL on the rear side (right side).

Figures 1a-c show cross-sectional scanning electron micrographs (SEM) of the investigated PSTSC device configurations: The reference PSTSC device (Fig. 1a) features a fully planar front

side (upper half) and a standard random pyramid texture at the rear side of the silicon heterojunction (SHJ) subcell (lower half). The reference solar cell is similar to that presented in our previous publications[1] and consists of a SHJ solar cell with *n*-doped hydrogenated nanocrystalline silicon oxide [nc-SiO_x:H (n)], doped indium oxide as TCO, a self-assembled monolayer (SAM, Me-4PACz), a mixed-cation and mixed-halide perovskite absorber, lithium fluoride (LiF), C_{60}, tin oxide, indium zinc oxide (IZO) and LiF. The perovskite composition is either $Cs_{0.05}(FA_{0.79}MA_{0.21})_{0.95}Pb(I_{0.79}Br_{0.21})_3$ or $(Cs_{0.05}(FA_{0.77}MA_{0.23})_{0.95}Pb(I_{0.77}Br_{0.23})_3$ with bandgap energies of 1.66 eV or 1.68 eV, respectively.

The sinusoidal nanostructure at the front surface of the silicon subcell (Fig. 1b and c) was manufactured by combining UV nanoimprint lithography, reactive ion etching and wet chemical etching[28]. The experimental procedure is detailed in the Methods Section. The resulting nanotexture has a hexagonal lattice with a period of 750 nm and a peak-to-valley height of approximately 300 nm (Fig. 1d). This nanotexture can be completely covered by the perovskite film with a typical thickness of 500-600 nm (on planar surfaces) revealing a flat perovskite front surface on the C_{60} side. At the rear side of the silicon wafer we applied a reflector with a dielectric buffer layer (RDBL)[30] (Fig. 1c). The RDBL comprises of a SiO_2 buffer layer between the TCO and the silver (Ag) back reflector. This allows to reduce the TCO thickness and to increase the distance between Ag and the absorber, reducing parasitic absorption both in the TCO and in the metal. An Ag grid covering 4% of the active area is screen-printed on top of the TCO before SiO_2 deposition to establish the electric contact between the TCO and Ag (Fig. 1e, right side).

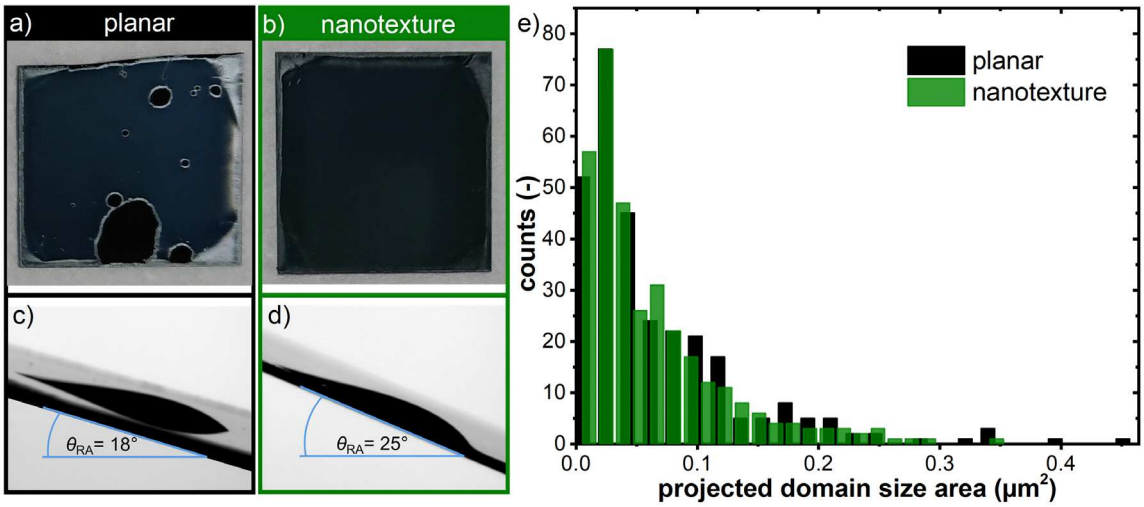

Figure 2 | Perovskite film formation and morphology. a, b) Representative spin-coated perovskite films on planar (a) and nanotextured (b) silicon bottom cells covered by Me-4PACz (area approximately 1 inch x 1 inch). c), d) Corresponding side-view photographs of perovskite-solution droplets with the roll-of-angle (RA) indicated. e) Projected domain area of perovskite layers deposited on planar and nanotextured substrates as determined from top-view SEM images (see Fig. S2).

Perovskite film formation and morphology

Although Me-4PACz improves the electronic properties (e.g. compared to 2PACz and PTAA), the suboptimal formation of perovskite films on planar bottom cells/Me-4PACz often leads to macroscopic holes (Fig. 2a) and therefore to a low yield of working devices. However, when the perovskite is spin-coated onto Me-4PACz-covered nanotextured silicon bottom cells (Fig. 2b), the occurrence of holes is greatly reduced: Out of 45 processed nanotextured tandem solar cells only two had visible holes after perovskite spin-coating (~95% yield). In contrast, out of 30 planar devices, which were processed in parallel to the nanotextured cells, 15 showed macroscopic holes (~50% yield). To get a more systematic understanding of this observation, we measured the roll-off angle (Fig. 2c,d), which is defined as the tilting angle at which a droplet of perovskite solution starts to roll off the surface[31]. On the nanotextured sample, we observe a larger roll-off angle (25°) than for the planar reference (18°), indicating the improved ability of the surface to retain the perovskite solution. This observation can be explained from the approach of de Gennes *et al.*, in which the resulting droplet retention force is enhanced by surface roughness pinning the three-phase contact line[32,33].

To further study the morphological properties of perovskite layers grown onto sinusoidal nanotextures, we captured SEM top view images (Fig. S2), and analyzed the projected domain size distribution as depicted in Fig. 2e. The domain size distribution is equal with a mean equivalent disk radius of 130 ± 60 nm and 120 ± 60 nm for planar and nanotextured silicon bottom cells, respectively. This is not surprising as it was reported that with the antisolvent method the crystallization is initiated at the top surface, which is not affected by the buried nanotextured interface[34].

Optical analysis

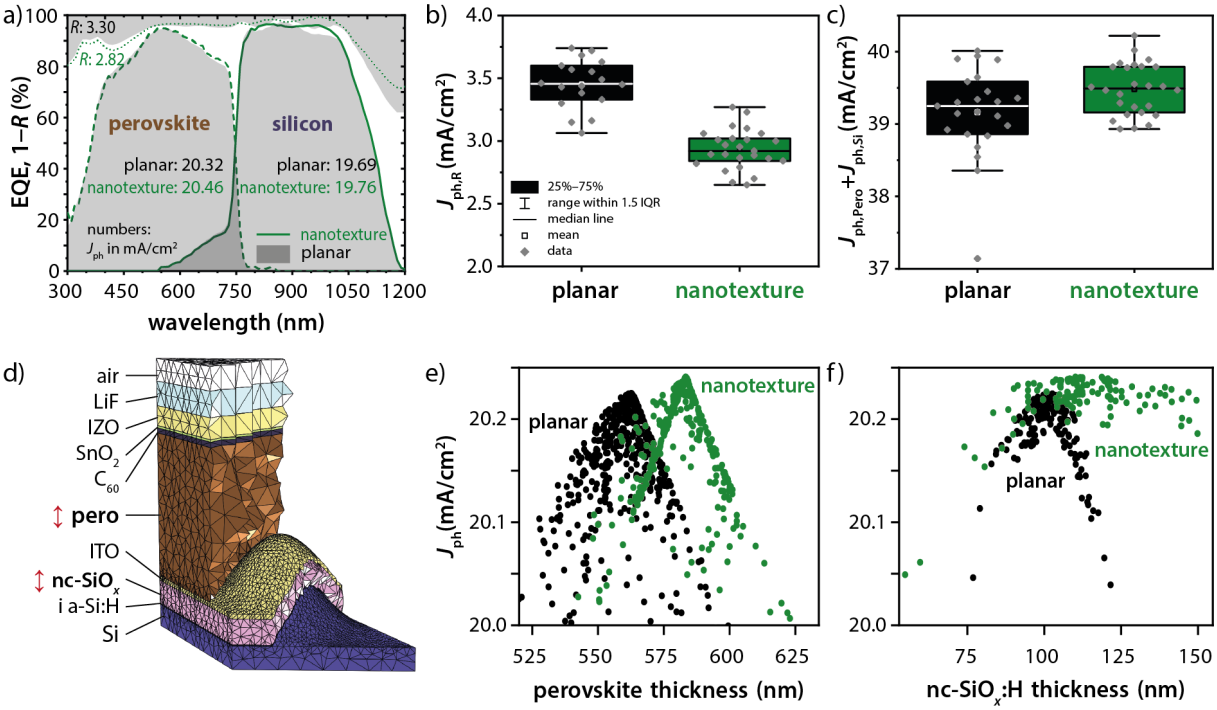

Figure 3 | Optical analysis of nanotextures in perovskite/silicon tandem solar cells (PSTSCs). a) Representative experimental external quantum efficiency (EQE) and 1-reflection (1-*R*) spectra for a typical pair of planar (gray areas) and nanotextured (green lines) PSTSCs with standard rear reflector (no RDBL). b,c) Box plot diagrams of integrated current density from experimental reflection measurements ($J_{ph,R}$) and sum of integrated current densities in the perovskite and silicon subcell from EQE measurements ($J_{ph,Pero}$+$J_{ph,Si}$). The planar and nanotextured PSTSCs are displayed in black and green boxes, respectively. d) Cross section through a meshed unit cell of a PSTSC with nanotextures between perovskite and silicon sub cells, as used for simulations with the finite element method. e,f) Sensitivity analysis for different layers, based on optical simulations: minimum of photogenerated current densities min[J_{ph}(pero),J_{Si}(pero)] as a function of perovskite (e) and nc-SiO_x:H (f) layer thickness for planar (black dots) and nanotextured (green dots) PSTSCs. In (e), the perovskite thickness for the nanotextured device is defined as the thickness of a planar layer with the same overall volume. For clarity, in (f) only data for samples with a perovskite thickness within ±5 nm of the optimal perovskite thickness are shown.

The optical performance of the planar and nanotextured PSTSCs was analyzed with external quantum efficiency (EQE) and reflectance (R) measurements. Representative EQE and $1-R$ spectra for planar (gray areas) and nanotextured (green lines) PSTSC are displayed in Fig. 3a: No significant difference can be observed in the EQE of the perovskite; the integrated current densities ($J_{ph,Pero}$) are 20.32 and 20.46 mA/cm² for planar and nanotextured, respectively. In contrast, the EQEs of the silicon subcells differ from each other: the nanotexture diminishes peaks and valleys caused by thin-film interference (green solid line), which occurs within the perovskite top cell. Here, the integrated current density ($J_{ph,Si}$) of the silicon EQEs are comparable with 19.69 (planar) and 19.76 (nanotextured) mA/cm², respectively. In contrast to the EQE measurements, nanotexturing reduces reflectance considerably from 3.30 to 2.82 mA/cm² current-density-equivalent. All these findings are reproduced when considering a larger amount of processed PSTSC devices (Fig. 3b+c): the integrated current density of the reflection spectra ($J_{ph,R}$) in a boxplot diagram (Fig. 3b) confirms the nanotexture-induced reduction of reflectance by around 0.5 mA/cm^2 current-density-equivalent on average. The statistical analysis of the combined photogenerated current density ($J_{ph,Pero}$+$J_{ph,Si}$) from EQE measurements yields highest values for selected nanotextured devices confirming their optical potential. The average values are 39.15 mA/cm^2 and 39.47 mA/cm^2 for the planar and nanotextured devices, respectively, confirming the benefit of nanotextures on the optical device performance (Fig. 3c). The partial compensation of optical gain as expected from reflectance might be attributed to a larger spread of electronic performance of the nanotextured silicon bottom cells, partly revealing a slightly lower internal quantum efficiency compared to their planar counterparts (Fig. S3). Nonetheless, the overall high level of optical performance was independently confirmed by the EQE calculated from the relative spectral response measurements at Fraunhofer ISE CalLab (see Fig. S4a,b for certificate and EQE spectra) with photogenerated current densities of 20.31 and 19.70 mA/cm² for perovskite and silicon subcells of a nanotextured PSTSC, respectively. The combined photogenerated current density of 40.01 mA/cm² is among the highest values reported in the literature for 2-terminal PSTSCs. Higher values have only been demonstrated with fully textured PSTSC (see Fig. S5)[15,18,20].

In view of process robustness we performed a numerical sensitivity analysis to study the influence of layer thicknesses in the top cell on the photogenerated current density. We used data sets obtained during a Bayesian optimization based on the finite element method (FEM)

similar to previous work[14]. Figure 3d shows a cross section through a meshed unit cell of a PSTSC with nanotextures between perovskite and silicon subcells, as is used in the FEM simulations. During the Bayesian optimization, the overall current density of the monolithic tandem device was optimized by maximizing the minimum of the two subcell photocurrent densities, i.e. the value of $\min[J_{\mathrm{ph,Pero}}, J_{\mathrm{ph,Si}}]$ is maximized. Note that these simulations assume perfect Lambertian light trapping at the rear side of the silicon bottom cell without any parasitic absorption such that the following results mainly concern the perovskite top cell layer design. The results of the sensitivity analysis are shown in Fig. 3e and 3f as functions of the perovskite and nc-SiO_x:H (n) layer thickness, respectively. According to these simulations, the optimized nanotextured PSTSC performs almost similar as the optimized planar device with matched photogenerated current densities of 20.24 mA/cm^2 and 20.22 mA/cm^2, respectively. As seen in Fig. 3e, the sensitivity to a changing perovskite thickness is also similar for the planar and nanotextured designs. This is plausible because the current-density distribution between perovskite and silicon is directly linked to the perovskite volume, which is controlled by the perovskite thickness. However, texturing reduces the sensitivity to a changing nc-SiO_x:H(n) thickness, as seen in Fig. 3f: while for planar devices the photocurrent density peaks at around 100 nm nc-SiO_x:H(n) thickness, for the nanotextured design the photocurrent density reaches a plateau for nc-SiO_x:H(n) layers thicker than 100 nm. This means that nanotexturing of the PSTSC widens the process window for the optical nc-SiO_x:H(n) interlayer, which is an important aspect for industrialization of the tandem technology especially when processing on larger areas.

Optoelectronic analysis

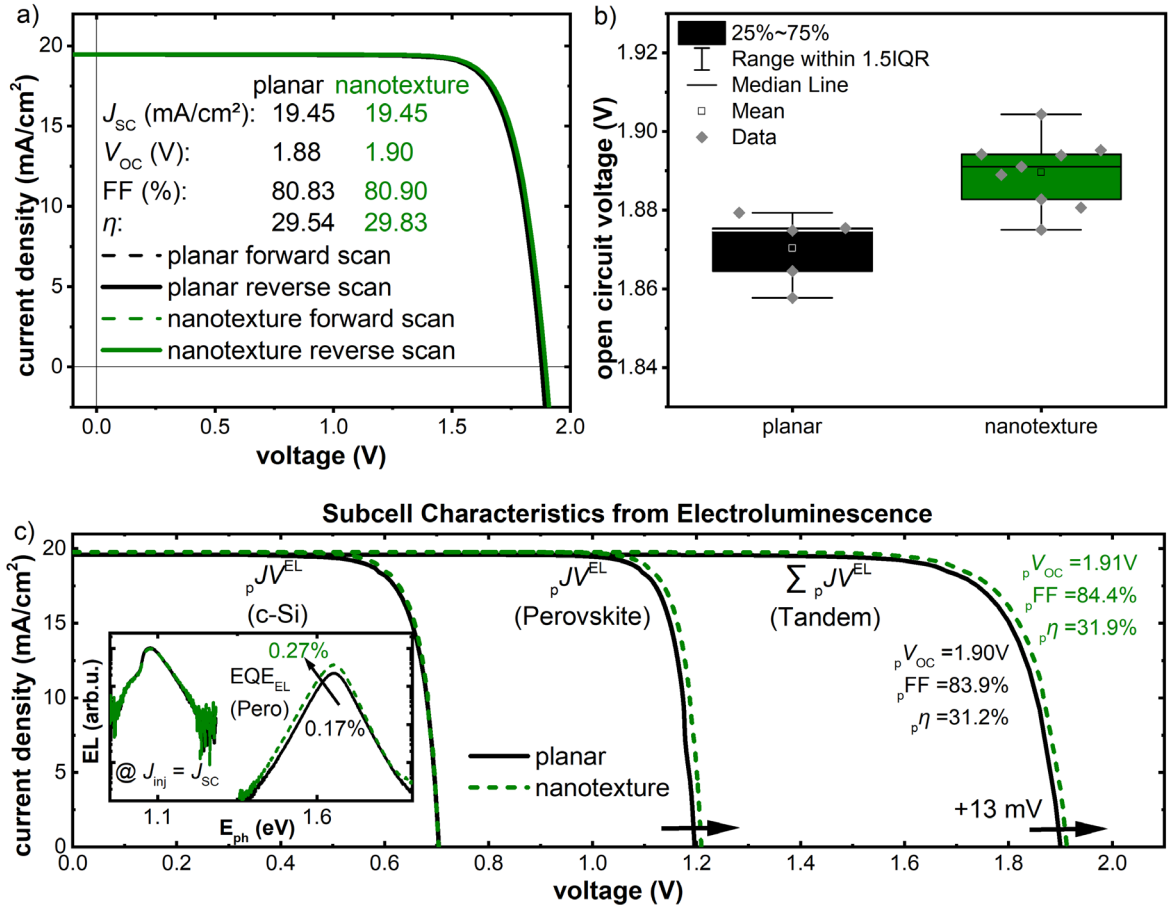

Figure 4 | Solar cell characteristics of nanotextured perovskite/silicon tandem solar cells (PSTSCs). a) Representative current-density/voltage (*JV*) characteristics of planar and nanotextured PSTSC. b) Box plot of open-circuit voltage for planar and nanotextured PSTSC with perovskite bandgap energy of 1.68 eV. c) pseudo-*JV* characteristics of planar and textured PSTSC showing the individual c-Si and perovskite subcells via subcell selective electroluminescence (EL) measurements. The inset visualizes the EL spectra at $J_{inj.} = J_{SC}$ conditions.

Figure 4a shows the current-density/voltage characteristics of representative nanotextured and planar PSTSCs. Both devices show PCEs above 29% with a J_{SC} of 19.45 mA/cm². Note, that the fill factor (*FF*) of the planar and nanotextured PSTSC shows similar values, too. Even when considering many devices and the influence of current density mismatch ($J_{ph,Pero} - J_{ph,Si}$) on the *FF*[7], no clear difference can be observed between the planar and nanotextured configurations (Fig. S6). Next to the electronic characteristics, we tested the stability at maximum power point by subjecting both, a planar and nanotextured PSTSC, to continuous illumination in a dedicated tandem aging setup. The observed degradation over time (Fig. S7) resembles previous results[1]. So far, we see no impact on stability by implementing the nanotextures. In contrast, the open-circuit voltages (V_{OC}) of planar and nanotextured PSTSC differ significantly. As this enhancement is rather small, we investigated the statistical distribution of planar and nanotextured PSTSCs to draw reliable conclusions. Figure 4b displays the open-circuit voltages

(V_{OC}) of planar (black box) and nanotextured (green box) PSTSC with a perovskite bandgap of 1.68 eV (data from the same batch to eliminate process differences). The overall V_{OC} distribution shows higher maximum values and a statistical improvement of the median V_{OC} by around 15 mV for nanotextured compared to planar PSTSCs. To verify and understand this effect, we used a subcell-selective characterization approach based on electro- and photoluminescence (EL/PL), which allows to assess the charge transport and recombination properties of the top and bottom cell and to determine their efficiency potential. First, we quantified the injection-dependent electroluminescence quantum yield (EQE_{EL}) of both subcells by injecting a current into the tandem device and detecting the emitted EL of both subcells. From the emitted EL, we calculated the quasi-Fermi level splitting $(\mathrm{QFLS_{EL}})$. The injection-dependent $\mathrm{QFLS_{EL}}$ equals a series-resistance-free dark *JV* curve, from which we can generate a pseudo-*JV* curve by adding the generation current[35,36]. Figure 4c shows the obtained characteristics of both subcells in the tandem configuration for the planar and nanotextured PSTSC. These results reveal an approximately ~60% enhanced EQE_{EL} in the perovskite subcell in case of the nanostructured PSTSC (Fig. S8), which explains the ~15 mV V_{OC} gain in the corresponding *JV*-measurements. Further, the EL emission of perovskite in the nanotextured devices is slightly skewed (inset of Fig. 4c) which might suggest enhanced photon-recycling[37]. We note that the implied performance of both Si subcells is identical and that the obtained efficiency potential in case of the nanostructured device is almost 32%, which could be realized upon improving the charge extraction from the perovskite and/or from the transport layers. The EQE_{EL}/V_{OC} of the perovskite on the nanotextured silicon cell might have increased because of an improved optoelectronic quality of the absorber layer, slightly lower non-radiative recombination losses at the interfaces, or an alteration of the optical coupling between the perovskite and the Si.

Record tandem solar cells with optically advanced rear reflector

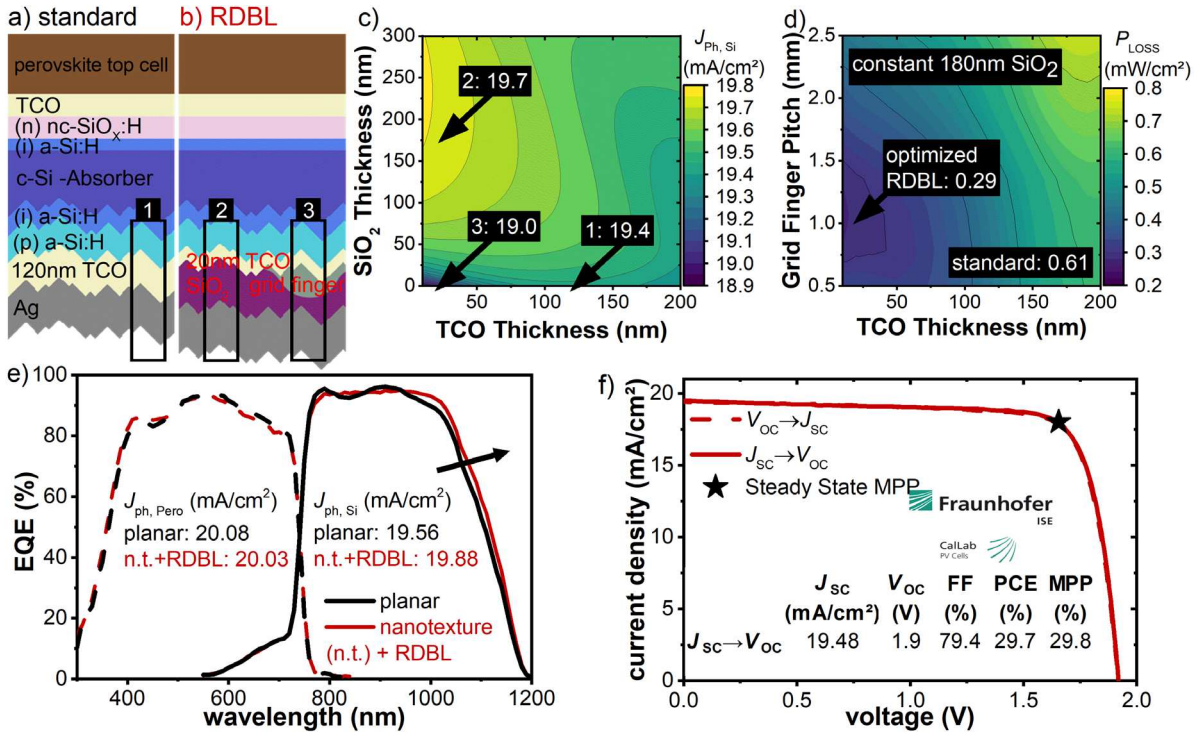

Figure 5 | Implementing a rear reflector with dielectric buffer layer (RDBL) for record nanotextured perovskite/silicon tandem solar cells (PSTSCs). a,b) Schematic of the PSTSC layer stack with standard reflector (a) and with RDBL at the rear side (b). The black frames with annotated numbers mark the standard rear side (1) and the SiO_2 (2) and grid finger (3) regions of the RDBL. c) 2D map of $J_{ph,Si}$ for different SiO_2 (*y*-axis) and TCO thicknesses (*x*-axis), calculated with the software GenPro4[38]. The configurations corresponding to the experimental layer stacks are marked with arrows and the corresponding $J_{ph,Si}$ is indicated. d) 2D map of power losses in the Si bottom cell for different grid finger pitches (*y*-axis) with 40 µm finger width and TCO thicknesses, calculated with Quokka3 software[39]. The RDBL configuration is marked with an arrow and the corresponding power loss in mW/cm² is provided. The power loss for the standard reflector is indicated in the inset. e) External quantum efficiency (EQE) spectra of planar PSTSC with standard rear side (black) and nanotextured PSTSC with RDBL (red). The integrated photogenerated current densities of perovskite ($J_{ph,Pero}$) and silicon ($J_{ph,Si}$) are displayed in the graph. f) Current-density/voltage (*J*-*V*) characteristics of a nanotextured PSTSC with RDBL certified by CalLab at Fraunhofer ISE. The maximum power point (MPP) value is marked as a black star.

To reduce parasitic absorption losses in the rear reflector, we additionally implemented a reflector with dielectric buffer layer (RDBL), as recently employed in silicon heterojunction single-junction solar cells at HZB[30]. Figure 5a and b illustrate PSTSC layer stacks with standard reflector and with RDBL, respectively. Three optically different regions can be distinguished: 1—Standard reflector (120 nm TCO, no buffer layer), 2—RDBL (20 nm TCO, 180 nm SiO_2 buffer layer) and 3—Grid fingers of the RDBL (20 nm TCO, no buffer layer). SEM images of the corresponding regions are presented in Fig. S9. To quantify the optical properties of these

three regions, we performed simulations of the photogenerated current density in te silicon ($J_{ph,Si}$) in dependence of the TCO and the SiO_2 thickness, using the software GenPro4[38] (see Fig. 5c). For the optimized layer thicknesses, the photocurrent density of the silicon bottom cell $J_{ph,Si}$ increases from 19.4 to 19.7 mA/cm² when replacing the standard reflector design (region 1) by the RDBL (region 2) mostly due to reduced parasitic absorption in the TCO/Ag contact and as a result an increased absorption in the silicon bandedge region. A full-area design as in the grid finger (region 3) would lead to $J_{ph,Si}$ of 19.0 mA/cm².

Finally, the local contact area has to be optoelectronically optimized not only considering the optical properties, but also lateral transport and contact resistive losses. This means that the TCO thickness as well as the grid finger geometry have to be balanced. Figure 5d shows the simulation results using the software Quokka3[39]. (Details can be found in the Methods Section). It is observed that the power loss decreases with TCO thickness reduction, since the benefit from reduced parasitic absorption dominates. For an Ag-grid finger width of 40 µm we find an optoelectrical optimum for a grid pitch of roughly 1.1 mm (Fig. 5d). Hence, a finger pitch of 1 mm was implemented, resulting in local contacts covering roughly 4% of the active area. The optoelectronic analysis further shows that the power can be increased by 0.45 mW/cm² with respect to the reference device due to enhanced $J_{ph,Si}$ by the RDBL (assuming a current matched tandem cell). Increased resistive losses reduce this gain slightly by 0.15 mW/cm², such that overall the RDBL potentially increases the power output by 0.3 mW/cm². The EQE spectra of experimentally realized PSTSC with and without a RDBL are shown in Fig. 5e. In addition to the flattening of the silicon EQE, which arises from the nanotextures, the EQE spectra of the PSTSC with RDBL features an increased absorption at the band edge of silicon, as expected from the optical simulations. To account for the additional current density from the RDBL in the silicon sub-cell, we shifted the perovskite bandgap from 1.68 eV to 1.66 eV. One of the best PSTSC featuring both, a nanotextured interface between the perovskite and silicon sub cell and a RDBL, was sent to Fraunhofer ISE CalLab for independent certification (Fig. 5f; see Fig. S10 for certificate). The cell reached a PCE of 29.75% when measured from J_{SC} to V_{OC} (designated area of 1.0163 cm^2), with a V_{OC} of 1.92 V, *FF* of 79.4%, and a J_{SC} of 19.56 mA/cm². The certified PCE, as determined from maximum power point (MPP) tracking, is 29.80%. This PCE surpasses other two- and four-terminal PSTSC and performs even better than the best single-junction solar cell (GaAs)[2].

Conclusions

In this study, we integrated gentle sub-micrometer-periodic nanotextures and an improved back reflector design into monolithic perovskite/silicon tandem solar cells. The nanotextures enable improved perovskite film formation properties and, in this way, greatly enhanced process yield of the solution-processed perovskite top cell from around 50% in case of planar to about 95% for nanotextured silicon bottom cells. We further observed a reduction of reflection losses amounting to around 0.5 mA/cm² current-density-equivalent. As a result, combined short-circuit current densities in the perovskite and silicon subcells of up to 40.0 mA/cm^2 are observed, which is among the highest values reported in the literature for 2-terminal perovskite/silicon tandem solar cells. A sensitivity analysis employing optical finite element method simulations and a Bayesian optimization algorithm further indicates that the nanotextures substantially reduce the sensitivity of the tandem cells to deviations from the optimal nanocrystalline silicon oxide layer thickness - an important aspect with regard to the industrialization of tandem technology and processing on larger areas. The main driver for improved PSTSC performance was an increase of the open-circuit voltage by around 15 mV, that stems, according to our subcell-selective EL characterizations, solely from an improved perovskite-top-cell performance. In addition to the nanotextures at the silicon bottom cell front-side, we further implemented a reflector with dielectric buffer layer (RDBL) at the rear side. This design further improves the current density in the silicon bottom cell by around 0.3 mA/cm² by reducing parasitic absorption losses in the TCO and in the silver reflector. By combining nanotextures and RDBL in one PSTSC, we achieved a certified power conversion efficiency of 29.80%. These results pave the way for a wide use of nano-optical designs in high-efficient perovskite solar cells and other metal halide perovskite optoelectronic devices in the near future.

Materials and Methods

Device Fabrication

Nanotextured silicon bottom cells: A three-step process, developed by Sutter *et al.*[28], was used to implement nanotextures into silicon wafers for perovskite/silicon tandem solar cells (PSTSC). Sinusoidal master structures, manufactured by laser interference lithography[40], were replicated by nanoimprint lithography (NIL) with a polydimethylsiloxane (PDMS) stamp into an UV-curable resist (mrNIL210-500, Microresist Technologies GmbH) on double side polished (100) silicon n-type float-zone wafer (Topsil) with a nominal resistivity of 1 – 5 Ω·cm and an approximate thickness of 280 µm.

For the NIL process, the 4 inch wafers were cleaned by standard RCA procedure[41]. In ambient condition, 700 µL of resist was spin-coated for 30 s at 3200 revolutions per minute (rpm) on the wafer, prebaked for 3 min at 60°C and cured by UV-light with the PDMS stamp comprising the inverted nanotexture from the master on top for 2 min. In a second step, the reproduced nanotexture was anisotropically etched into the silicon substrate by reactive-ion etching (RIE) with the etching gases sulfur hexafluoride (SF_6) and fluoroform (CHF_3) for 16 min at 90 W radio frequency (RF) power and 20 mTorr pressure. In this step, the nanotextured resist served as a 3D etching mask and allowed to replicate the texture into the underlying silicon. An additional RIE oxygen plasma was applied to eliminate organic residues. Due to the diffusion of ions and silicon lattice distortion, a subsequent wet-chemical defect etch with nitric acid, phosphoric acid and fluoric acid (HNO_3(65%)/H_3PO_4(85%)/HF(50%)/H2O [30:10:1:15]) was done. Prior to the texturing of the rear side with random pyramids with (111) facets (potassium-hydroxide etched, 8 min @ 83°C, CellTex Ultra as additive from ICB), the nanotextured front side was protected with a 320 nm thick PECVD-deposited SiO_2 layer. After removal of the capping in HF, a final RCA clean and HF dip (1% dilution in water) were done. Intrinsic and doped hydrogenated amorphous [a-Si:H (i)/a-Si:H (p)] and nanocrystalline silicon oxide [nc-SiOx:H (n)] layers were deposited by plasma enhanced chemical vapor deposition (PECVD) using an Applied Materials AKT1600 cluster tool. To account for the enhanced surface area, the process parameters for the front side of the nanotextured wafers were adapted by a factor of 1.3 with regard to the planar case. 20 nm doped indium oxide as transparent conductive oxide was sputtered as recombination contact. The rear-side contact of the silicon bottom cells consists of 120 nm for the standard design and 20 nm sputtered doped indium oxide (InO) for the reflector design with dielectric buffer layer (RDBL). The RDBL has an additional silver grid printed on the rear side with a nominal finger width of 40 µm and a 1 mm pitch, which was cured 10 min at 210°C, followed by a PECVD deposition of 180 nm SiO_2. For both, standard and RDBL rear-side designs, 400 nm silver was sputtered as back contact layer. All contacts of the silicon bottom cell were processed through a quadratic mask with 1.1 cm² area. After sputtering silver, the silicon wafers of the standard design were annealed for 10 min at 210°C and wafers of both designs were additionally annealed for 5 min at 210°C under 1-sun illumination. Then, the wafers were laser-cut into 2.5× 2.5 cm² pieces, with the 1.1 cm² area of the contact in the center.

For fabricating the perovskite top cells, we adapted a device stack reported earlier[1]. For cleaning, the 2.5 × 2.5 cm² silicon bottom cells were blown with N_2, ethanol (C_2H_5OH) was spincoated at 2500 rpm for 30 s, which was succeeded by UV-O_3-treatment for 15 min. Further processes were carried out in a nitrogen-filled glovebox. 100 µL of a 3 mM solution of Me-4PACz (TCI) were dissolved in C_2H_5OH and spin-coated (3000 rpm for 30 s) onto the bottom cells, followed by a 10 min annealing at 100°C. Then, either $Cs_{0.05}(FA_{0.79}MA_{0.21})_{0.95}Pb(I_{0.79}Br_{0.21})_3$ (1.66 eV bandgap) or $Cs_{0.05}(FA_{0.77}MA_{0.23})_{0.95}Pb(I_{0.77}Br_{0.23})_3$

(1.68 eV bandgap) perovskite was prepared, adapted from a recipe by Saliba *et al.*[42] For this, precursor solutions containing formamidinium iodide (FAI, Dyenamo) and lead iodide (PbI_2, TCI) were mixed in a ratio of 79:21 or 77:23 with a precursor solution containing methylammonium bromide (MABr, Dyenamo) and lead bromide ($PbBr_2$, TCI). Both precursor solutions contained 1 M of the corresponding organic and 1.1 M of the lead salts which were dissolved in a mixture of anhydrous DMF:DMSO 4:1 (vol:vol; both purchased from Sigma Aldrich). Further on, 5%$_{vol}$ cesium iodide (CsI, abcr) from a 1.5 M stock solution in DMSO was added to the precursor solutions. The resulting perovskite solution was then spin-coated at 3500 rpm for 40 s. 15 s prior to the end of the program, 500 µL ethyl acetate (EA, Sigma Aldrich) was poured on the spinning substrate. The films were annealed at 100°C for 30 min. The front-side contact was deposited through subsequent thermal evaporation of 1 nm lithium fluoride (LiF, Sigma Aldrich) and 18 nm C_{60} (Sigma Aldrich). Then, 20 nm tin oxide (SnO_2) by thermal atomic layer deposition (ALD) in an Arradiance GEMStar reactor were depostied at 80°C. 100 nm indium zinc oxide (IZO) 150 W, Ar/O_2 mixture were deposited by sputtering. A 100 nm silver frame was thermally evaporated through a shadow mask to collect the charge carriers without a need of grid fingers. Finally, 100 nm LiF were thermally evaporated as an antireflective coating. The active area is defined by the metal frame and is slightly larger than 1 cm².

Characterization

Roll-off measurements were conducted using a contact angle goniometer (DSA 25, Krüss). In all measurements, 10 µl droplets of perovskite solution (see above) were used. For the roll-off angle measurements the samples were placed on fixed, inclined stages before dispensing the solution. The here used methodology allows the qualitative analysis in the droplet retention behavior of both planar and textured surfaces[43].

Reflectance was measured under an angle of 8° in 5 nm steps from 300 to 1200 nm with a PerkinElmer Lambda–1050+ UV/VIS/NIR spectrophotometer, which was calibrated with a Spectralon. For statistics on reflectance of PSTSC, perovskite absorber with bandgaps varying from 1.66 eV to 1.68 eV were used.

Atomic force microscopy (AFM) measurements were performed with a XE-70 AFM (Park Systems). For accurate profile scans in the nanometer regime high aspect ratio tips were used. Scanning electron microscopy (SEM) was performed with a MERLIN Field Emission Scanning Electron Microscope with a GEMINI II optical column from Zeiss.

Electroluminescence Measurements (EL): Absolute EL measurements were performed using a calibrated Si photodetector and a Keithley 485 picoamperemeter. The detector (with ~1 cm^2 active area) was placed directly in front of the device, and the total photon flux was evaluated considering

the emission spectrum of the perovskite and silicon subcell, and the EQE of the detector. To selectively pick up EL from the perovskite or c-Si subcell, appropriate longpass and shortpass filters were used. Underestimation of the $\mathrm{EQE_{EL}}$ due to not detected photons that escaped to the side was compensated by additional measurements at different distances and with a larger detector (active area $\sim$2 cm^2). During a typical EL measurement, a Keithley 2400 source meter was used to apply a forward bias to the cell, and the injected current was monitored. Measurements were conducted with a home-written LabVIEW routine. Relative EL spectra of the perovskite/silicon tandem solar cell were measured with an Andor SR393i-B spectrometer equipped with an Andor iDus silicon CCD camera and an iDus InGaAs detector array. The spectral response of the system was calibrated by using a calibrated halogen lamp with specified spectral irradiance. The quasi-Fermi level splitting $(\mathrm{QFLS_{EL}})$ was calculated according to $\mathrm{QFLS_{EL}} = k_\mathrm{B}T * \ln\left(\mathrm{EQE_{EL}} * \frac{J_\mathrm{G}}{J_{0,rad}}\right)$, where $k_\mathrm{B}T$ is the thermal energy at room temperature, and $J_{0,\mathrm{rad}}$, J_G the radiative recombination current in the dark, and the 1−sun-equivalent (AM1.5G) generation current, respectively. The quantification of the $J_{0,\mathrm{rad}}$ of both sub cells is shown in Fig. S11, and Table S1.

Solar cell characteristics: The tandem solar cells were measured in air under AM1.5G (1 sun) equivalent illumination with a Wavelabs Sinus-70 LED class AAA solar simulator as described in a previous publication by Al-Ashouri *et al.*[1]. The cells were not preconditioned. For calibration we used a slightly modified calibration routine as described in reference [44]. We adjusted the spectrum such that it led to the photogenerated current densities obtained by EQE measurements for both subcells. Thus, for a perovskite-limited cell, we first increased the intensity of the blue light in order to get a silicon-limited cell. Subsequently, the NIR region was adjusted until the J_{SC} of the silicon-limited tandem solar cell was equal to the $J_{ph,Si}$ (calculated from EQE and AM1.5G spectrum). Finally, the intensity of the blue light was decreased until the tandem solar cell was perovskite-limited again and the J_{SC} was equal to the $J_{ph,Pero}$. For a silicon-limited cell it is done vice versa. The backside of the cell was contacted with a metal vacuum chuck at 25°C, whereas the front side was contacted with two Au probes. A black laser-cut aperture mask covered the substrate outside of the active area. The *J-V* measurements and MPP tracks were recorded using a home-built LabView software. The EQE spectra were recorded with a home-built setup using chopped (79 Hz) monochromatic light from a Xe and He lamp, respectively. To measure the EQE of the perovskite subcell, the silicon subcell was saturated using an LED with 850 nm peak emission. To maintain short circuit conditions, a bias voltage of 0.6 V was applied. The silicon subcell was measured by saturating the perovskite subcell with blue light from a LED (455 nm) and applying a bias voltage of 1.0 V. For statistics on totalized integrated sub-cell current densities of PSTSC, perovskite absorber with bandgaps varying from 1.66 eV to 1.68 eV were used.

Simulations

3D Optical Simulations JCMwave and Bayesian Optimization

The data for sensitivity study presented in Fig. 3 was generated during a layer-thickness optimization with a Bayesian optimization algorithm[45], similar to an optimization we presented in previous work[14]. During the optimization the thicknesses of the perovskite and nc-SiO_x:H layers were varied in order to maximize the function $\min[J_{\mathrm{ph,pero}}, J_{\mathrm{ph,Si}}]$, which is a well-suited optimization function for monolithic tandem solar cells, as it directly accounts for current matching[46]. The individual simulations were performed with the finite element method (FEM) solver JCM suite[47] for a 300 - 1190 nm wavelength range and produced absorption spectra for all the layers of the solar cell stack. To be able to do the FEM simulations, we had to restrict the simulation domain to the perovskite top cell and to assume the silicon to be infinitely thick. To compensate, we corrected the absorption of the silicon layer by assuming perfect light trapping for the silicon wafer according to Tiedje and Yablonovitch[48]. From the absorption spectra, the photocurrent densities were calculated; see e.g. Ref. [46]. Details on the layer thicknesses, optical material data and optimization results are given in Table S2 in the Supporting Information.

1D Optical Simulations GenPro

The optical simulations on the reflector with dielectric buffer layer (RDBL) shown in Fig. 5c were performed with GenPro4 developed by TU Delft[38], which uses the net-radiation method and ray tracing for scattering at the pyramidal back side of the solar cell. Details on the layer stack used for these simulations are given in Table S3 in the Supporting Information.

Optoelectrical simulations Quokka

For the RDBL with local contacts, the TCO sheet resistance (R_{Sheet}) depending on its electrical properties and thickness as well as the grid fingers depending on their pitch, geometry and resistivity have to be optimized. To calculate this balance, electrical simulations were carried out with the Quokka3 software[39] for which we assumed the wafer properties, finger geometry and resistivity as well as the Si/TCO/Ag contact resistivities to remain constant. Note as well that the TCO R_{Sheet} does not increase linearly with thickness reduction since we considered the variation of its electrical properties in the real solar cell-like structures as studied in Ref. [30]. The reference point from which the optical power loss (P_{Loss}) is calculated J_{SC}= 19.73 mA/cm² at t_{TCO} = 10 nm and *FP* = 2.5 mm and decreases up to 19.44 at t_{TCO} = 200 nm and *FP* = 0.5 mm. For this J_{SC} range variation V_{OC} = 1.9 V and *FF* = 79.52% are assumed to remain constant. In the case of the electrical P_{Loss} the holes, vertical, lateral, and metal fingers transport losses are calculated assuming constant J_{SC} = 19.4 mA/cm². Further parameters used can be found in Table S4 of the Supporting Information.

Acknowledgements

The authors wish to thank J. Beckedahl, C. Ferber, M. Gabernig, and H. Heinz for technical support in the HySPRINT lab and I. Rudolph for technical support in the BESSY cleanroom. C. Klimm and K. Sveinbjörnsson are acknowledged for SEM measurements. K. Jacob is acknowledged for RCA cleaning of silicon wafers and technical support. The authors thank F. Riesebeck for support during the Poly-Si etching. K. Mayer-Stillrich, M. Hartig and D. Debrassine are recognized for sputtering of TCO layers and F. Biegalke for KOH etching. C. Trinh is acknowledged for PECVD deposition and J. Kleesiek for screen printing.

Funding was provided by German Federal Ministry for Education and Research (BMBF) through grant no. 03SF0540 and the SNaPSHoTs Project (grant no. 01IO1806), the German Federal Ministry for Economic Affairs (BMWi) through the "PersiST" project (grant no. 0324037C) and "PrEsto" project (grant no. 03EE1086C), the HyperCells Graduate School, the HI-SCORE Research School, and the HySPRINT Helmholtz Innovation Lab. Further, this work was supported by the Helmholtz Association within the EU-Partnering project TAPAS (Tandem Perovskite and Silicon Solar Cells Advanced Optoelectrical Characterization, Modelling and Stability) and the Helmholtz Excellence Network SolarMath, a strategic collaboration of MATH+ and Helmholtz-Zentrum Berlin (Grant No. ExNet-0042-Phase-2-3). We acknowledge funding by the Deutsche Forschungsgemeinschaft (DFG) under Germany's Excellence Strategy (EXC-2046/1, Project ID: 390685689, MATH+ AA4-6). M.S. acknowledges the Deutsche Forschungsgemeinschaft (DFG, German Research Foundation) - project number 423749265 - SPP 2196 (SURPRISE) and financial support by the Federal Ministry for Economic Affairs and Energy (P3T-HOPE, 03EE1017C) for funding.

References

1. Al-Ashouri, A. *et al.* Monolithic perovskite/silicon tandem solar cell with >29% efficiency by enhanced hole extraction. *Science* **370**, 1300–1309 (2020).
2. Green, M. A. *et al.* Solar cell efficiency tables (version 59). *Progress in Photovoltaics: Research and Applications* **30**, 3–12 (2021).
3. Richter, A., Hermle, M. & Glunz, S. W. Reassessment of the Limiting Efficiency for Crystalline Silicon Solar Cells. *IEEE J. Photovoltaics* **3**, 1184–1191 (2013).
4. Bush, K. A. *et al.* Compositional Engineering for Efficient Wide Band Gap Perovskites with Improved Stability to Photoinduced Phase Segregation. *ACS Energy Lett.* **3**, 428–435 (2018).
5. Bush, K. A. *et al.* Minimizing Current and Voltage Losses to Reach 25% Efficient Monolithic Two-Terminal Perovskite-Silicon Tandem Solar Cells. *ACS Energy Letters* **3**, 2173–2180 (2018).

6. Mazzarella, L. *et al.* Infrared Light Management Using a Nanocrystalline Silicon Oxide Interlayer in Monolithic Perovskite/Silicon Heterojunction Tandem Solar Cells with Efficiency above 25%. *Advanced Energy Materials* **9**, 1803241 (2019).
7. Köhnen, E. *et al.* Highly efficient monolithic perovskite silicon tandem solar cells: analyzing the influence of current mismatch on device performance. *Sustainable Energy Fuels* **3**, 1995–2005 (2019).
8. Chen, B. *et al.* Grain Engineering for Perovskite/Silicon Monolithic Tandem Solar Cells with Efficiency of 25.4%. *Joule* **3**, 177–190 (2019).
9. Kim, D. *et al.* Efficient, stable silicon tandem cells enabled by anion-engineered wide-bandgap perovskites. *Science* **368**, 155–160 (2020).
10. Isikgor, F. H. *et al.* Concurrent cationic and anionic perovskite defect passivation enables 27.4% perovskite/silicon tandems with suppression of halide segregation. *Joule* **5**, 1566–1586 (2021).
11. Xu, J. *et al.* Triple-halide wide–band gap perovskites with suppressed phase segregation for efficient tandems. *Science* **367**, 1097–1104 (2020).
12. Schulze, P. S. C. *et al.* 25.1% High-Efficiency Monolithic Perovskite Silicon Tandem Solar Cell with a High Bandgap Perovskite Absorber. *Sol. RRL* **4**, 2000152 (2020).
13. Santbergen, R. *et al.* Minimizing optical losses in monolithic perovskite/c-Si tandem solar cells with a flat top cell. *Optics Express* **24**, A1288 (2016).
14. Jäger, K., Sutter, J., Hammerschmidt, M., Schneider, P.-I. & Becker, C. Prospects of light management in perovskite/silicon tandem solar cells. *Nanophotonics* **10**, 1991–2000 (2020).
15. Sahli, F. *et al.* Fully textured monolithic perovskite/silicon tandem solar cells with 25.2% power conversion efficiency. *Nature Materials* **17**, 820–826 (2018).
16. Nogay, G. *et al.* 25.1%-Efficient Monolithic Perovskite/Silicon Tandem Solar Cell Based on a *p* -type Monocrystalline Textured Silicon Wafer and High-Temperature Passivating Contacts. *ACS Energy Lett.* **4**, 844–845 (2019).
17. Aydin, E. *et al.* Interplay between temperature and bandgap energies on the outdoor performance of perovskite/silicon tandem solar cells. *Nature Energy* **5**, 851–859 (2020).
18. Tennyson, E. M. *et al.* Multimodal Microscale Imaging of Textured Perovskite–Silicon Tandem Solar Cells. *ACS Energy Letters* **6**, 2293–2304 (2021).
19. Roß, M. *et al.* Co-Evaporated Formamidinium Lead Iodide Based Perovskites with 1000 h Constant Stability for Fully Textured Monolithic Perovskite/Silicon Tandem Solar Cells. *Advanced Energy Materials* **11**, 2101460 (2021).
20. Li, Y. *et al.* Wide Bandgap Interface Layer Induced Stabilized Perovskite/Silicon Tandem Solar Cells with Stability over Ten Thousand Hours. *Advanced Energy Materials* **11**, 2102046 (2021).

21. Subbiah, A. S. *et al.* High-Performance Perovskite Single-Junction and Textured Perovskite/Silicon Tandem Solar Cells via Slot-Die-Coating. *ACS Energy Letters* **5**, 3034–3040 (2020).
22. Chen, B. *et al.* Blade-Coated Perovskites on Textured Silicon for 26%-Efficient Monolithic Perovskite/Silicon Tandem Solar Cells. *Joule* **4**, 850–864 (2020).
23. Hou, Y. *et al.* Efficient tandem solar cells with solution-processed perovskite on textured crystalline silicon. *Science* **367**, 1135–1140 (2020).
24. Zhumagali, S. *et al.* Linked Nickel Oxide/Perovskite Interface Passivation for High-Performance Textured Monolithic Tandem Solar Cells. *Advanced Energy Materials* **11**, 2101662 (2021).
25. Santbergen, R. *et al.* Ray-optics study of gentle non-conformal texture morphologies for perovskite/silicon tandems. *Opt. Express* **30**, 5608 (2022).
26. Chen, D. *et al.* Nanophotonic light management for perovskite–silicon tandem solar cells. *Journal of Photonics for Energy* **8**, 022601 (2018).
27. Tockhorn, P. *et al.* Improved Quantum Efficiency by Advanced Light Management in Nanotextured Solution-Processed Perovskite Solar Cells. *ACS Photonics* **7**, 2589–2600 (2020).
28. Sutter, J. *et al.* Tailored Nanostructures for Light Management in Silicon Heterojunction Solar Cells. *Solar RRL* **4**, 2000484 (2020).
29. Holman, Z. C. *et al.* Infrared light management in high-efficiency silicon heterojunction and rear-passivated solar cells. *Journal of Applied Physics* **113**, 013107 (2013).
30. Cruz, A. *et al.* Optoelectrical analysis of TCO$\mathplus$Silicon oxide double layers at the front and rear side of silicon heterojunction solar cells. *Solar Energy Materials and Solar Cells* **236**, 111493 (2022).
31. Bhushan, B., Jung, Y. C. & Koch, K. Micro-, nano- and hierarchical structures for superhydrophobicity, self-cleaning and low adhesion. *Philosophical Transactions of the Royal Society A: Mathematical, Physical and Engineering Sciences* **367**, 1631–1672 (2009).
32. Joanny, J. F. & Gennes, P. G. de. A model for contact angle hysteresis. *The Journal of Chemical Physics* **81**, 552–562 (1984).
33. Tadmor, R. Open Problems in Wetting Phenomena: Pinning Retention Forces. *Langmuir* **37**, 6357–6372 (2021).
34. Minemawari, H. *et al.* Inkjet printing of single-crystal films. *Nature* **475**, 364–367 (2011).
35. Stolterfoht, M. *et al.* How To Quantify the Efficiency Potential of Neat Perovskite Films: Perovskite Semiconductors with an Implied Efficiency Exceeding 28%. *Adv. Mater.* **32**, 2000080 (2020).
36. Lang, F. *et al.* Revealing Fundamental Efficiency Limits of Monolithic Perovskite/Silicon Tandem Photovoltaics through Subcell Characterization. *ACS Energy Lett.* **6**, 3982–3991 (2021).

37. Cho, C. *et al.* Effects of photon recycling and scattering in high-performance perovskite solar cells. *Sci. Adv.* **7**, eabj1363 (2021).
38. Santbergen, R. *et al.* GenPro4 Optical Model for Solar Cell Simulation and Its Application to Multijunction Solar Cells. *IEEE Journal of Photovoltaics* **7**, 919–926 (2017).
39. Fell, A. A Free and Fast Three-Dimensional/Two-Dimensional Solar Cell Simulator Featuring Conductive Boundary and Quasi-Neutrality Approximations. *IEEE Transactions on Electron Devices* **60**, 733–738 (2013).
40. Wolf, A. J. *et al.* Origination of nano- and microstructures on large areas by interference lithography. *Microelectronic Engineering* **98**, 293–296 (2012).
41. Kern, W. The Evolution of Silicon Wafer Cleaning Technology. *Journal of The Electrochemical Society* **137**, 1887–1892 (1990).
42. Saliba, M. *et al.* Cesium-containing triple cation perovskite solar cells: improved stability, reproducibility and high efficiency. *Energy & Environmental Science* **9**, 1989–1997 (2016).
43. Pierce, E., Carmona, F. J. & Amirfazli, A. Understanding of sliding and contact angle results in tilted plate experiments. *Colloids and Surfaces A: Physicochemical and Engineering Aspects* **323**, 73–82 (2008).
44. Meusel, M., Adelhelm, R., Dimroth, F., Bett, A. W. & Warta, W. Spectral mismatch correction and spectrometric characterization of monolithic III-V multi-junction solar cells. *Prog. Photovolt: Res. Appl.* **10**, 243–255 (2002).
45. Schneider, P.-I., Garcia Santiago, X., Rockstuhl, C. & Burger, S. Global optimization of complex optical structures using Bayesian optimization based on Gaussian processes. in (eds. Kress, B. C., Osten, W. & Urbach, H. P.) 103350O (2017). doi:10.1117/12.2270609.
46. Jäger, K., Korte, L., Rech, B. & Albrecht, S. Numerical optical optimization of monolithic planar perovskite-silicon tandem solar cells with regular and inverted device architectures. *Opt. Express* **25**, A473 (2017).
47. Pomplun, J., Burger, S., Zschiedrich, L. & Schmidt, F. Adaptive finite element method for simulation of optical nano structures. *phys. stat. sol. (b)* **244**, 3419–3434 (2007).
48. Tiedje, T., Yablonovitch, E., Cody, G. D. & Brooks, B. G. Limiting efficiency of silicon solar cells. *IEEE Trans. Electron Devices* **31**, 711–716 (1984).

Supplementary Files

This is a list of supplementary files associated with this preprint. Click to download.

- nrphotovoltaicreporting.pdf
- SupportingInformation.pdf